Chemical Engineering Journal 462 (2023) 142227

Contents lists available at ScienceDirect

Chemical Engineering Journal

journal homepage: www.elsevier.com/locate/cej

Methane coupling in nanosecond pulsed plasmas: Correlation between temperature and pressure and effects on product selectivity

Eduardo Morais [a,1], Evangelos Delikonstantis [b,c,1], Marco Scapinello [c], Gregory Smith [a], Georgios D. Stefanidis [c,d,*], Annemie Bogaerts [a,*]

[a] PLASMANT, Department of Chemistry, University of Antwerp, Wilrijk-Antwerp 2610, Belgium
[b] AristEng S.à r.l., 77, rue de Merl, L-2146 Luxembourg City, Luxembourg
[c] Laboratory for Chemical Technology, Ghent University, Tech Lane Ghent Science Park 125, Ghent B-9052, Belgium
[d] School of Chemical Engineering, National Technical University of Athens, Iroon Polytechniou 9, 15780 Athens, Greece

ARTICLE INFO

Keywords:
Methane
Ethylene
Plasma
Kinetic model
Electrification

ABSTRACT

We present a zero-dimensional kinetic model to characterise specifically the gas-phase dynamics of methane conversion in a nanosecond pulsed discharge (NPD) plasma reactor. The model includes a systematic approach to capture the nanoscale power discharges and the rapid ensuing changes in electric field, gas and electron temperature, as well as species densities. The effects of gas temperature and reactor pressure on gas conversion and product selectivity are extensively investigated and validated against experimental work. We discuss the important reaction pathways and provide an analysis of the dynamics of the heating and cooling mechanisms. H radicals are found to be the most populous plasma species and they participate in hydrogenation and dehydrogenation reactions, which are the dominant recombination reactions leading to C_2H_4 and C_2H_2 as main products (depending on the pressure).

1. Introduction

Given the current energy crisis, the societal and industrial importance of natural gas as a primary energy source and feedstock will be significant in the coming decennia. Methane (CH_4), the most abundant compound of natural gas, can be converted stepwise to synthetic fuels via syngas. Alternatively, methane can be converted to valuable chemicals that serve as high added-value building blocks in the chemical industry. Among them, ethylene (C_2H_4) has the highest market value since it is the basic building block for a very broad range of chemicals, including polymers, synthetic fibres, alcohols, and solvents. Thus, scalable and energy-efficient processes to convert methane to ethylene are of high research interest.

Ethylene derives from natural gas via thermally driven (catalytic) oxidative or non-oxidative methane coupling. The oxidative coupling of methane is an exothermic reaction occurring at 1000–1200 K, usually in presence of catalyst. Along with ethylene, other lower-value side-products, such as carbon dioxide (CO_2), carbon monoxide (CO), hydrogen (H_2) and water (H_2O), are formed, restricting the application prospects of this route. Unlike oxidative methane coupling, non-oxidative coupling promotes the formation of high-value species, *i.e.*, ethane (C_2H_6), ethylene (C_2H_4) and acetylene (C_2H_2), hydrogen, benzene (C_6H_6) and other aromatics at appropriate temperatures and in presence of suitable catalysts. Carbon and hydrogen are thermodynamically favoured between 1500 and 3300 K; benzene between 1100 and 1500 K; acetylene at higher temperatures, whereas ethylene production is maximized between 1300 and 1800 K [1,2].

Besides thermally-driven routes [3], electrified options have also been proposed for non-oxidative methane coupling [4]. In this context, plasma is employed to enable the reaction. Specifically, non-thermal plasma (NTP) can electrically activate methane molecules at lower bulk gas temperatures than pyrolysis, maximizing the conversion of electrical into chemical energy and subsequently, improving the global energy efficiency. Different plasma technologies, *i.e.*, dielectric barrier discharges (DBD) [5,6], microwave (MW) [7], gliding arc (GA) [8], spark and corona [9,10], have been tested for methane reforming. In low-energy density plasmas (DBD), ethane is formed as the major product, whereas acetylene formation dominates in high-energy density

* Corresponding authors.
E-mail addresses: gstefani@mail.ntua.gr (G.D. Stefanidis), annemie.bogaerts@uantwerpen.be (A. Bogaerts).
[1] The authors have equally contributed to this work.

https://doi.org/10.1016/j.cej.2023.142227
Received 21 October 2022; Received in revised form 10 January 2023; Accepted 27 February 2023
Available online 2 March 2023

discharges (MW, GA and spark). Ethylene selectivity is enhanced in corona discharges, yet the overall yield still remains low. Collectively, plasma is not very selective to ethylene unless it is integrated with catalysts suitable for acetylene hydrogenation to ethylene in the post-plasma zone [11]. The reason for the very broad product distribution lies in the different electron temperature and electron density each plasma technology features, which impose the operating temperature and consequently, drive the plasma chemistry.

The Nanosecond Pulsed Discharge (NPD), a spark-regime discharge that can sufficiently populate the desirable vibrational and electronic states while limiting translational excitation, has been lately adopted to methane valorisation applications, attaining high single-pass C_2 yields at relatively low energy cost [11–14]. Acetylene was always the major product, like in other high-energy density discharges, but the reaction mechanism has not been defined yet. Only limited works elaborating on methane plasma chemistry have been published; most of them exploring microsecond pulsed discharges, a similar but not the same plasma type as NPDs. Kado et al. [15] investigated the mechanism of acetylene formation in such discharges; they reported that methane is mainly dissociated via electron impact reactions into atomic carbon, which is then hydrogenated to C_2H and CH and finally, those species serve as the precursors for C_2H_2 formation under certain hydrogenation and recombination reactions. Gao et al. [16] suggested that methane vibrational excitation is the lead methane dissociation mechanism since the vibrational excitation cross section has the dominant role in the energy channelling. They also claimed that vibrational-translational/rotational relaxation promotes thermal methane coupling to C_2 and carbon when gas temperature overpasses 1100 K.

Recently, Stefanidis and co-workers reported for the first time in the literature that gas phase plasma-assisted non-oxidative methane coupling can lead to the formation of ethylene as major product in NPDs - attaining ~ 20% single-pass ethylene yield at 2020 kJ/mol_{C2H4} energy cost - when co-feeding recyclable hydrogen (CH_4:H_2 = 1:1) and operating at moderate pressures (3.5 – 5 bar) [17]. The reaction pathways that shifted the product selectivity from acetylene to ethylene were determined via an isotope analysis. It was found that higher bulk gas temperatures imposed by the overpressure (>3 bar) activate direct gas-phase methane coupling to ethylene and suggested that some acetylene hydrogenation to ethylene takes place at the copper-based reactor electrode [18].

In the current work, we aim to elucidate the correlation between temperature and pressure effects on C_2 products selectivity under different operating windows. First, we experimentally study the NPD plasma reactor performance in terms of methane conversion and C_2 selectivity in the pressure range of 1 to 5 bar. Further, we develop a zero-dimensional kinetic model to characterise the gas-phase dynamics of methane conversion in the NPD plasma reactor. The model includes a systematic approach to capture the nanoscale power discharges and the rapid ensuing changes in electric field, gas and electron temperature, as well as species densities. The effects of gas temperature and reactor pressure on gas conversion and product selectivity are extensively investigated and validated against the experimental work. Finally, we discuss the important reaction pathways and provide an analysis of the dynamics of the heating and cooling mechanisms.

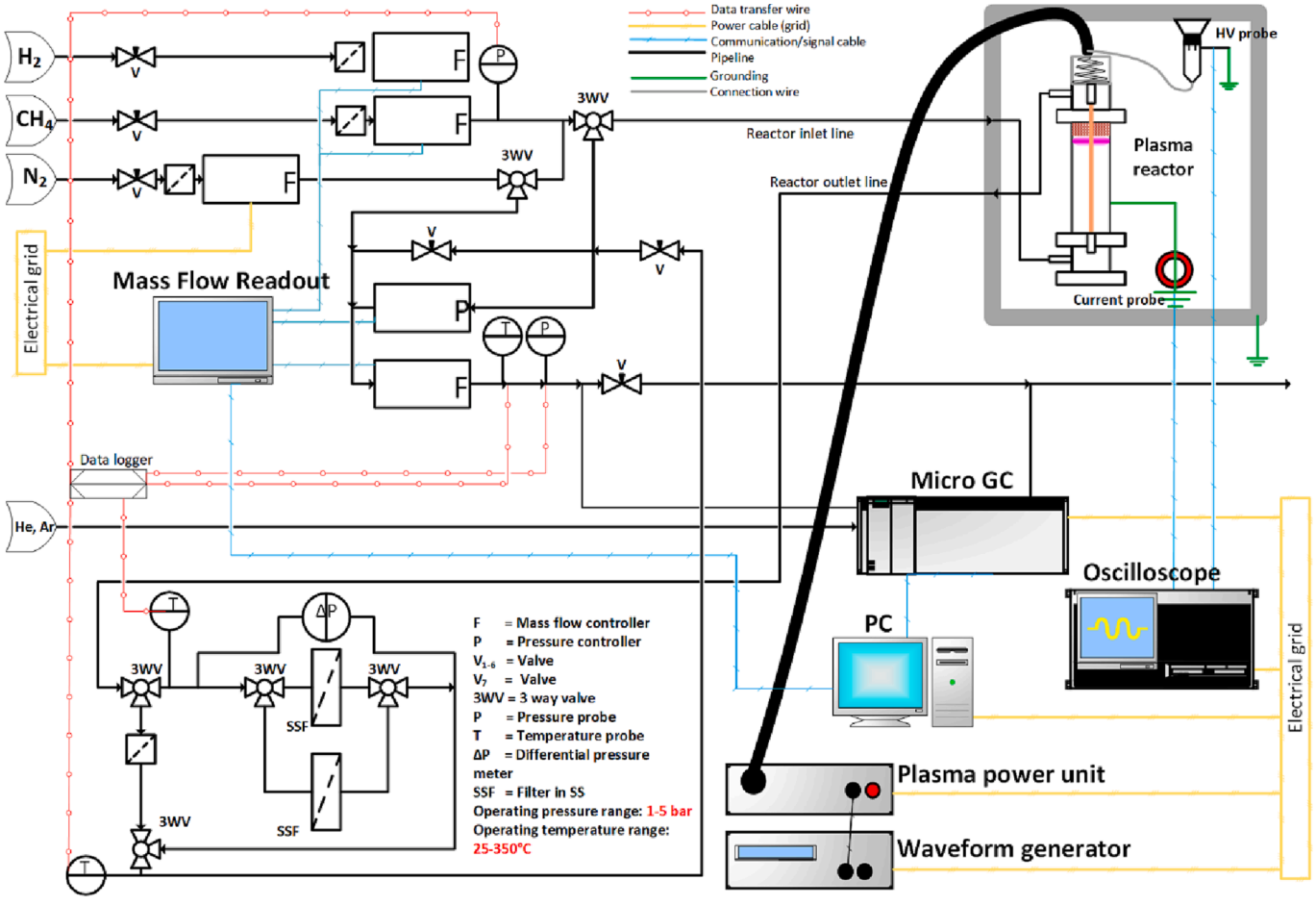

Fig. 1. Schematic representation of the experimental setup used for the non-oxidative methane coupling experiments, showing the plasma reactor and laboratory equipment, as well as the gas network with indications of flow directions, feeding points and line connections.

2. Experimental and computational methodology

2.1. Nanosecond pulsed plasma setup

The experimental setup used for the plasma-assisted non-oxidative methane experiments is presented in Fig. 1. The discharge was ignited by a nanosecond pulsed power supply (n-PS) (NPG-18/100 k, Megaimpulse Ltd.) which was triggered by a waveform generator (WFG) (33220A, Keysight Technology) at 3 kHz pulse repetition frequency. Based on a parametric study previously conducted [19], a pulse repetition frequency of 3 kHz led to an optimum performance with respect to single-pass conversion and energy efficiency. A high-voltage probe (P6015A Tektronix, 75 MHz bandwidth) and an I/V converter (CT-D-1.0, Magnelab, 200 Hz-500 MHz bandwidth) were used for the pulse voltage and current measurement, respectively. Voltage and current signals were recorded over the course of the experiment by a digital oscilloscope (Wavesurfer 10, Teledyne Lecroy) with a sampling frequency of 10 Gs/s. The pulse energy (E pulse) was estimated as elsewhere [20]. It equals the integral of the instantaneous power (V × I), considering the voltage (V) and current (I) signals time delay. The voltage and current signals time delay was calculated by zeroing the V × I product time integral in the absence of plasma, managed by filling the plasma reactor with SF_6. [21] Optical access to the discharge was not possible, however, representative pictures of the nanosecond pulsed discharge can be found in our previous work. [19].

The co-axial plasma reactor consisted of an inner, copper-based, axial wire (2.2 mm diameter) and an outer, stainless steel-based, coaxial tube (10.4 mm and 13 mm internal and external diameter, respectively). The inner axial wire constituted the high voltage (HV) electrode of the reactor while the outer coaxial tube constituted the ground electrode (GE) of the reactor. The interelectrode distance (plasma gap) and the coaxial plasma reactor length were 4.2 mm and 25 cm, respectively. The mixture of the reactants was fed through the bottom of the reactor (reactor inlet line) and the reactor effluent exited from the top of the reactor (reactor outlet line).

Mass flow controllers (GF40 Series, Brooks Instrument) controlled the feed flow rate of the reactants (100 sccm CH_4 and 100 sccm H_2; Air Liquide 99.995% purity). A filter (SS-4TF-7, Swagelok) with 7-μm pore size was installed at the plasma reactor outflow to retain the formed carbon. A differential pressure meter (Model 700.02, WIKA) was used to monitor the differential pressure across the filter cloth, which was cleaned when the differential pressure gauge exceeded a certain value. The plasma reactor pressure was regulated by using a pressure flow controller (SLA5820, Brooks Instrument) that was placed after the filter. A third mass flow controller (GF40 Series, Brooks Instrument), which was operated as flowmeter, continuously recorded the volumetric flowrate of the plasma reactor effluent. However, the readout value depends on a gas factor, which varied with the gas composition. Since the latter was not constant over the course of the plasma reaction, N_2 (Air Liquide, 99.999% purity) was used as internal standard to accurately measure the volume of the plasma reactor effluent. A known amount of N_2 (5 sccm) was only fed to the plasma reactor effluent (not inside the plasma zone over the course of the reaction) [22]. The three-way valve (3WV) was positioned in a manner such that N_2 was not allowed to flow through the plasma reactor along with the reactants, instead it drove the N_2 flow towards the reactor effluent. The outlet flow rate was obtained by multiplying the initial total flowrate ($CH_4 + H_2 + N_2$) by the ratio of the chromatographic area of N_2 before and during the plasma. An additional mass flow controller (4800 series, Brooks Instrument) was used to set the internal standard N_2 flow. The mass flow controllers were configured accordingly, and the respective gas factors were set before setting up of the experiments. The mass flow controllers for CH_4 and N_2 supply were set by default only for CH_4 and N_2 handling. Pressure probes (P1600 and P1650, Pace Scientific) and thermocouples (PT 900 Pace scientific) were employed to monitor the reactor operating conditions.

The analysis of the plasma reactor product stream was performed by an on-line GC (3000 MicroGC, Inficon). H_2, N_2 and CH_4 were detected by a molesieve column (10 m) with backflush (3 m, Plot U), while for C_2 species a Plot U column (10 m) with backflush (1 m, Plot Q) was used.

The following metrics were assessed to evaluate the plasma reactor performance: CH_4 conversion, C_2 selectivity and power input:

$$CH_4 \text{ conversion} = \left(1 - \left(\frac{[CH4]_{out} xv_{out}}{[CH4]_{in} xv_{in}}\right)\right) x100\% \quad (1)$$

$$C_2H_x \text{ selectivity} = \frac{2x[C_2H_x]_{out} xv_{out}}{[CH_4]_{in} xv_{in} - [CH_4]_{out} xv_{out}} x100\% \quad (2)$$

$$\text{Power input (MW)} = E_{pulse} x \left(\frac{MJ}{pulse}\right) xf \left(\frac{pulses}{s}\right) \quad (3)$$

where $[\ldots]_{in}$ and $[\ldots]_{out}$ correspond to CH_4 concentration at the plasma reactor feed and effluent stream, respectively, while ν_{in} and ν_{out} correspond to the corrected volumetric flowrates.

2.2. Plasma-kinetic model

(a) Numerical details

Our zero-dimensional kinetic model was constructed using the ZDPlasKin kinetic solver [23], which operates by evaluating the continuity differential equation for each chemical species s with number density $n_s(t)$ considered in the model:

$$\frac{dn_s}{dt} = \sum_r C_{r,\,s} k_r \prod_q n_q \quad (4)$$

where $C_{r,\,s}$ is the stoichiometric coefficient of a given species s in reaction r, k_r is the rate coefficient of reaction r and q is the colliding species in this process. Reactions which do not involve electron collisions use rate coefficients k_r from literature. k_r was given within a temperature range and written as a function of gas temperature where such data existed. In the case of electron impact reactions, k_r was extracted from continuous evaluation of collisional cross sections and the Electron Energy Distribution Function (EEDF) via the BOLSIG + solver. BOLSIG + operates in tandem with ZDPlasKin and requires electric field as input to derive the EEDF, from which the mean electron energy is determined, to then return rate coefficients for electron impact reactions [24]. The electric field E, required by BOLSIG + to solve the Boltzmann equation, is calculated via the differential of the Joule heating equation

$$\frac{dP}{dV} = \boldsymbol{J}.\boldsymbol{E} = \sigma E^2 \quad (5)$$

in which P is the power deposited in a volume element V, J (or σE) is the current density and σ is the electron conductivity, which is calculated by $\sigma = en_e\mu_e$ (e being the elementary charge, n_e the electron number density and μ_e the electron mobility, calculated by BOLSIG +) [24].

Neglecting any spatial dependence, the reduced electric field *(E/N)* is determined from the power density $p \equiv P/V$ as

$$\left(\frac{E}{N}\right) = \frac{1}{N}\sqrt{\frac{P}{\sigma}} \quad (6)$$

with N being the total number density of species in the gas phase.

(b) Power input

The power discharges were integrated in the model as power density, defined by the ratio of instantaneous power and volume of the plasma region. The instantaneous power contained in the discharges was determined using the experimental voltage and current profiles, whilst the volume of the plasma region in the reactor was assumed to be

constant for the duration of the pulses [17]. The power density was defined as a function of time using linear functions to generate asymmetrical triangular power pulses (shown in section 3.2 below). This definition considered the intensity and nanoscale width or duration of each individual pulse, as well as pulse frequency and operational duty cycle. In the theoretical framework of this model, this approach allowed for an accurate representation of the plasma discharges and their variation with the applied pressure in the reactor. These were measured by current and voltage probes during the experiments and are shown in the Supporting Information (SI, section 2) [17,20]. In the interest of model stability and physicality, the concept of a minimum power density between the pulses (*i.e.* plasma off period) was introduced to maintain the electron density and the electric field within viable ranges for model operation.

(c) **Gas temperature**

Calculations of gas temperature variation with time were performed self-consistently using the reaction enthalpies included in the model [25]. As the gas temperature T_{gas} (in Kelvin) can be assumed to be the same for all neutral species, only the adiabatic isometric heat transport equation needs to be solved: [23]

$$N\frac{yk}{y-1}\frac{dT_{gas}}{dt} = Pe,el + \sum jR_j\Delta H_j - P_{ext} \quad (7)$$

where $N = \sum n_i$ is the total neutral species density, γ is the specific heat ratio of the total gas mixture,*k* is the Boltzmann constant (in J K^{-1}), *Pe, el* is the gas heating power density due to elastic electron-neutral collisions (in W m^{-3}), R_j is the rate of reaction *j* (in m^{-3} s^{-1}), ΔH_j is the heat released (or consumed when this value is negative) by reaction *j* (in J) and P_{ext} is the heat loss due to energy exchange with the surroundings (in W m^{-3}). A detailed description of the gas temperature calculations is given in the SI (section 3).

(d) **Gas expansion**

Certain reactions in the chemistry of CH_4 conversion involve the formation of two molecules from one molecule. These reactions cause gas expansion, affecting the pressure and flow rate, which are calculated from the actual species density, velocity and gas temperature. To ensure conservation of gas pressure and mass flow rate, the species densities (calculated using Eq. (4) and velocity are corrected at every time step to account for gas expansion. More details are given in Kozak and Bogaerts [25].

(e) **Assumed plasma volume and number of pulses per residence time**

Accurate kinetic (and fluid dynamic) modelling under plasma discharges, particularly for simulations carried out with self-consistent temperature calculations, at atmospheric pressures and using pulsed power sources, is a challenging task. In particular, to model pulsed discharges in a 0D framework, it was necessary to make assumptions about the plasma volume and the number of pulses experienced by the gas molecules during their residence time in the reactor [26,27]. Hence, the modeller needs to make some assumptions to run within a feasible time-scale. Here we describe these assumptions, as well as the limitations of the model.

The volume of the plasma discharges in this reactor configuration was estimated to be 3% of the total volume of the reactor at 1 bar. Provided that the NPD streamer (accurately approximated as a column) diameter can be ~ 0.3 mm[13] at these operating conditions and considering the total effective reactor volume to be the space defined by the NPD streamer diameter and the plasma reactor cross-section area (since the NPD streamer is erratically ignited around the HV electrode), only ~ 3% of the total effective reactor volume is occupied by the NPD streamer during each event. This volume was assumed to remain constant in the pressure range of 1 to 5 bar. The difference between the total volume of the reactor and the plasma region affects how many pulses are experienced by each gas molecule traversing the reactor within the residence time. Although the pulse frequency is set to 3 kHz in the experiments, it is obvious that molecules travelling through the reactor will not be exposed to 3000 power pulses in 1 s (even if this were their residence time in the reactor). This is because exposure to power discharges occurs only in the plasma region, since the pulses are contained within the plasma volume. Considering these factors, the model was adjusted to account for 15 pulses, as an approximation to the number of pulses experienced by the gas molecules in the reactor. In all cases this number of pulses was sufficient for the modelled results to remain unaltered after the twelfth pulse.

(f) **Conversion and selectivity**

The CH_4 conversion is calculated as follows:

$$\chi\,CH4(\%) = 1 - \frac{n_{CH4f}(cm^{-3})v_f(cms^{-1})}{n_{CH4i}(cm^{-3})v_i(cms^{-1})}\text{x}100\% \quad (8)$$

where n_{CH4i} and v_i are the initial CH_4 density and velocity, while n_{CH4f} and v_f are the final CH_4 density and velocity.

The hydrocarbon selectivity is calculated as follows:

$$S\,C_xH_y(\%) = \frac{xn_{CxHy}(cm^{-3})v_f(cms^{-1})}{n_{CH4i}(cm^{-3})v_i(cms^{-1}) - n_{CH4f}(cm^{-3})v_f(cms^{-1})}\text{x}100\% \quad (9)$$

with n_{CxHy} being the density of any given hydrocarbon in the steady state.

2.3. Chemistry included in the model

A mixture of CH_4 and H_2 at a 50/50 ratio was adopted as input gas, in order to compare with the experiments. The species included in the model comprise CH_4 and H_2 molecules in ground and some vibrationally excited states, C and H atoms, various compounded C_xH_y molecules, as well as the corresponding radicals and ions, as shown in Table 1. These species react with each other in a large number of reactions, as detailed in SI (sections 4 – 6). To develop this reaction set, we built upon the basis of an earlier publication by PLASMANT, which investigated the utilisation of different plasma sources in CH_4 conversion [28]. In this study, ionic processes were expanded, rates of recombination reactions were updated and H_2 VV interactions were corrected to include detailed balance. These modifications were carried out using rate coefficients procured from various sources in the literature. A complete list of the reactions and corresponding rate coefficients (including interactions between vibrational levels), as well as relevant citations, can be found in Tables S2–S5 in the SI.

Table 1
Species considered in the model.

Stable molecules	Radicals	Ions and electrons	Excited molecules
CH_4 H_2 C_2H_2 C_2H_4 C_2H_6 C_3H_6 C_3H_8 C_4H_{10} $C_{(s)}$	C C_2 C_3 H CH_3 CH_2 CH C_2H C_2H_3 C_2H_5 C_3H_5 C_3H_7 C_4H_9	H^+ H_2^+ H_3^+ C^+ C_2^+ CH^+ CH_2^+ CH_3^+ CH_4^+ CH_5^+ C_2H^+ $C_2H_2^+$ $C_2H_3^+$ $C_2H_4^+$ $C_2H_5^+$ $C_2H_6^+$ H^- CH^- CH_2^- electrons	Vibrational: H_2 (v = 1… 14) CH_4 (v = 1… 4) Electronic: H_2* and CH_4*

3. Results and discussion

3.1. Plasma reactor performance

A streamer-to-spark discharge was ignited which covered only a restricted volume inside the co-axial plasma reactor; it accounted for ~ 3% of the hollow-cylindrical shaped volume around the HV electrode, as defined by the streamer diameter and the plasma reactor cross-section area [13]. The limited plasma volume compared to the reactor cross section provided rapid product quenching: the products exiting the plasma zone were instantly mixed with the low-temperature unreacted gases; the bulk gas temperature abruptly dropped and consequently, undesirable side-reactions, *i.e.*, C_2 species decomposition to carbon and hydrogen, were inhibited. The quenching rates may have been enhanced by the repetitive ignition (in the order of nanosecond) of the spark. It is noted that reactions can also be enabled in the proximity of the plasma zone, at distances longer than that of the discharge diameter, due to the relatively high gas temperature [29]. Hydrogen was co-fed to suppress carbon and benzene formation and increase acetylene selectivity at the expense of methane conversion [30].

The reactor performance in the non-oxidative CH_4 conversion is presented in Fig. 2. Pressure increase incentivises the electron-molecule collision frequency and the electron mean energy. As the discharge pressure is increased, the system is driven to thermal equilibrium leading to a higher number of electron-molecule collisions, and resulting in lower electron mean energy, thereby less energetic collisions. Therefore, methane conversion is initially boosted from 30% to 45% as pressure rises from 1 to 4 bar. At 5 bar, there is a slight drop in methane conversion, due to the slightly lower discharge energy. Beyond 5 bar, the reduction of electron mean energy becomes significant and conversion is compromised.

Regarding product distribution, C_2H_2 is the dominant product when operating at atmospheric pressure. At 2 bar and higher pressures, C_2H_4 becomes the dominant product. The highest ethylene selectivity is attained at 5 bar. At this pressure, the C_2H_2 and C_2H_6 yields account for less than 5% of product distribution. This product selectivity shift can be attributed to the direct CH_2 radical coupling (with CH_3) to ethylene and C_2H_3 hydrogenation with H radicals – both reactions are enhanced by high bulk gas temperatures imposed by the overpressure (>3 bar) - as revealed by the isotopic analysis previously performed by Stefanidis and co-workers [18] and further explored in the reaction pathway analysis provided by the modelled results (section 3.5). Moreover, in pulsed plasmas, catalytic hydrogenation occurring at the surface of the copper-based HV electrode also has an effect on the improved C_2H_4 selectivity at higher pressures [18], owing to the ability of copper to promote C_2H_2 to C_2H_4 hydrogenation reactions [31]. In a future follow-up, we intend to expand this work to investigate this effect under these conditions both on experimental and computational fronts.

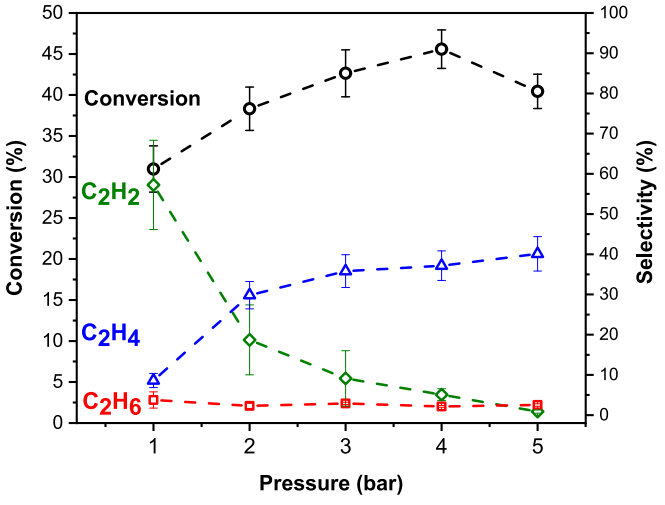

Fig. 2. NPD plasma reactor performance in terms of CH_4 conversion and C_2 selectivity across the 1 – 5 bar pressure range. Total feed rate: 200 sccm; gas feed composition: CH_4:H_2 = 1:1; frequency: 3 kHz; discharge gap: 2.4 mm.

3.2. Modelled plasma characteristics

In all calculations carried out in this study, the following parameters were kept constant: gas feed composition of CH_4:H_2 = 1:1, gas flow rate of 200 sccm, reactor dimensions (see section 2.1), pulse frequency of 3 kHz, number of modelled pulses as 15 pulses, initial gas temperature of 298.15 K and volume of the plasma region as 3% of the reactor volume [13]. This was done to highlight the effects of variations in the applied pressure (1 to 5 bar) and power input (and in turn gas and electron temperature), as well as to study how CH_4 conversion, product selectivity and reaction pathways respond to these different conditions of pressure and power input.

The time-resolved power density profiles constructed to emulate the pulsed plasma discharges at different pressures are shown in Fig. 3a. Each pulse is characterised by an asymmetrical triangle with shorter upslope (rise time) and longer downslope (fall time). In line with experimental power inputs (see Fig. S1), the intensity and width of the power density pulses in the model are pressure dependent, with the maximum power of each pulse rising with pressure and the width decreasing with increasing pressure, generating pulses with shorter duration (sharper triangles).

In Fig. 3b the 15 modelled pulses are plotted at different pressures. While the effect of pressure on pulse duration is not observable on the timescale of the residence time (ms), the different height of the power density pulses in the 1 to 5 bar pressure range is evident. The values of intensity and duration of the pulses for each pressure can be found in Table 2, alongside the calculated energy injected into the reactor per pulse. Table 2 also shows the total power deposited within the residence time, the maximum reduced electric field (E/N) reached at the top of the pulses and the average gas temperature in the afterglow estimated by the model at each pressure.

The energy (in mJ) channelled into the reactor per power pulse is reduced with rising pressure, as shown in Table 2. This effect is due to the pulses becoming shorter as the pressure is increasing (despite the higher intensity), resulting in less energy being deposited in the system with each pulse. This is obviously reflected in the total power (in W), which decreases with increasing pressure. The calculated values and the trend across the pressure range are in good alignment with experimental results (Fig. 4), especially in the mid pressure range, boding well for species density and temperature calculations carried out later in the model.

The response of the reduced electric field and in turn of the electron temperature to the power pulses is plotted in Fig. 5a. Akin to power density, the two profiles exhibit pulsed behaviour and the peaks in both are coincidental in time with the power discharges [32]. This is expected as the model computes the electric field from the power input, and in turn the electric field is supplied to BOLSIG + for EEDF calculations and electron temperature. The latter determine the energy of electrons in the plasma zone, which will initiate chemical reactions with the incoming CH_4 and H_2 molecules in the gas flow. Since the reduced electric field is inversely proportional to the density of gas-phase species, the maximum values calculated by the model (reached at the top of each power pulse) are reduced as the pressure is increased (Fig. 5b). This trend is also observed in the experimental values of the electric field (Fig. 5b), however these are somewhat lower than those calculated by the model. This is likely due to the nanosecond scale of the pulses, rendering precise acquisition of maximum electric field very difficult, and thus the values measured experimentally may be lower (*i.e.* with a relative delay) than those reached at the top of the power pulses [27]. The resulting calculated maximum electron temperature for each pressure is also plotted in

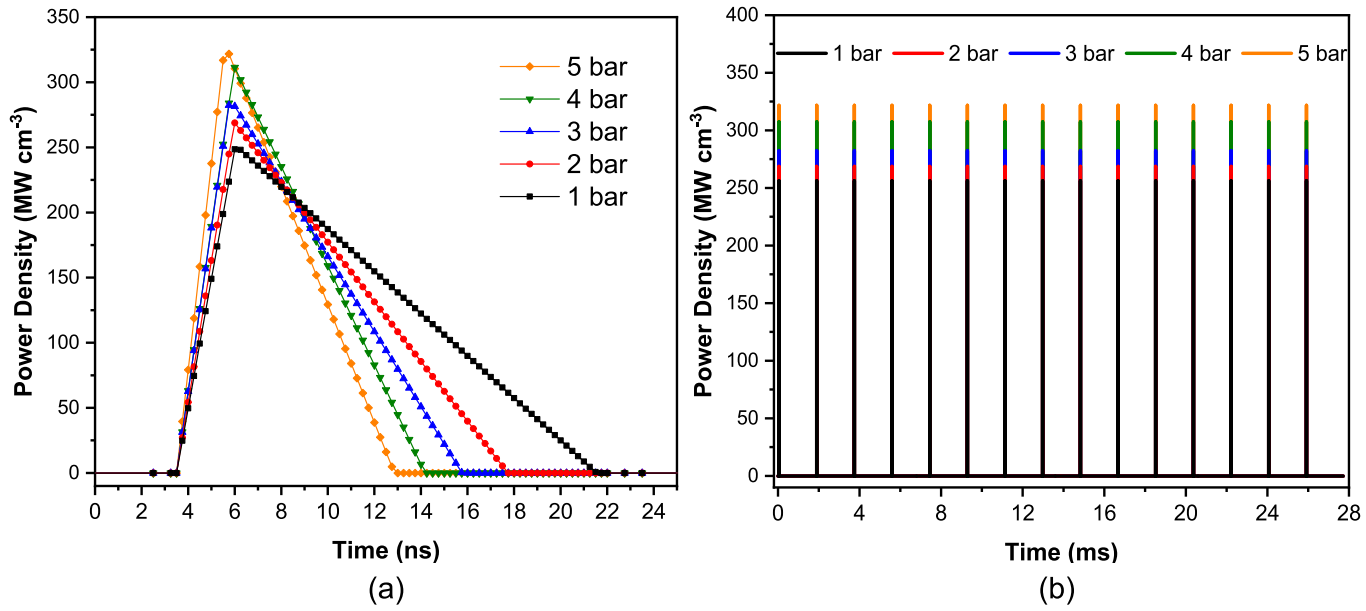

Fig. 3. (a) One asymmetrical triangular pulse at different pressures (1 to 5 bar) in the nanosecond range. The duration of the pulses varies from ~ 10 ns at 5 bar to 18 ns at 1 bar. (b) The 15 power pulses and afterglows modelled for the gas residence time (27.8 ms) in the reactor, corresponding to a gas flow rate of 200 sccm, as used in the experiments. The difference in width upon different pressure is not visible, but the different intensity of each pulse can be observed.

Table 2
Pulse characteristics, overall deposited power and calculated reduced electric field and average bulk gas temperature in the afterglow at different pressures.

Pressure (bar)	Pulse Characteristics			Power (W)	E/N max (Td)	T_{gas} (K)
	Intensity (MW cm^{-3})	Duration (ns)	Energy (mJ)			
1	251.7	18.0	26.4	14.3	347.5	1037.6
2	269.3	14.2	22.4	12.1	199.1	991.2
3	287.6	12.3	20.7	11.2	179.1	982.9
4	312.4	10.7	19.6	10.6	156.2	990.5
5	329.5	9.36	18.1	9.80	144.1	1074.0

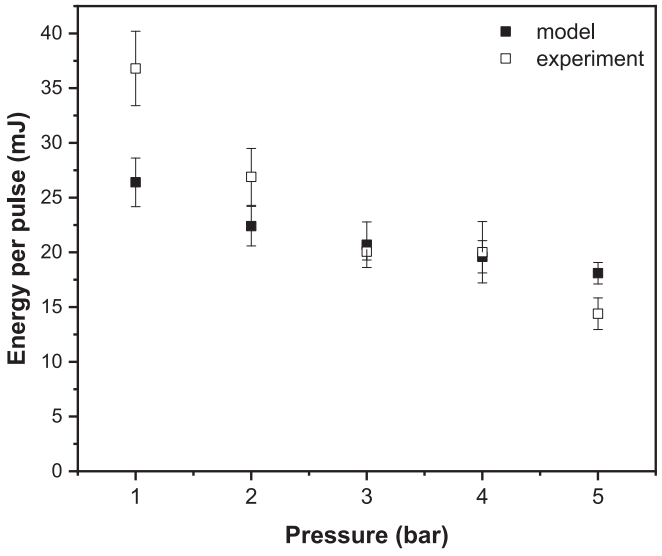

Fig. 4. Comparison between modelled and experimental energy per pulse deposited into the reactor across the pressure range studied. The modelled error bars are the standard deviation at each data point.

Fig. 5b, showing consistency with the trend in the reduced electric field.

Fig. 6 displays the profiles of gas temperature versus time for the different applied pressures as calculated by the 0D model (no experimental gas temperatures were measured). All profiles exhibit pulsed behaviour. While heating (leading to temperature peaks) occurs for ~ 120 ns after each power pulse, cooling begins subsequently and is a much slower process (resembling that of an exponential decay) as it takes place on the ms scale (~1.2 ms) during the afterglow until the next pulse. The heating and cooling dynamics derived from model calculations are presented and discussed in Section 3.6 below.

The amplitude of temperature variation (*i.e.* the difference between the calculated temperature at the top of each peak and at the very end of the subsequent afterglow) is inversely proportional to the applied pressure, with higher variations observed at lower pressures. Note that (i) the more intense E/N peaks and (ii) longer power depositions at lower pressures will both lead to the generation of more radicals whose recombination into stable molecules releases energy and heats the system following the power discharges. As the concentration of radicals is higher at lower pressures, more heating is experienced, resulting in more intense temperature peaks [33]. The difference in the amplitude of temperature variation as a function of pressure will be discussed in section 3.5.

In the afterglow, the time-averaged calculated gas temperature is similar at all pressures, around 1000 K, which is comparable to a report by Ravasio and Cavallotti for a similar system [33]. The calculated gas temperatures (T_{gas} = 1400 – 900 K, with an average of 1000 K) are starkly lower than the calculated electron temperatures (T_e = 39000 – 51000 K or 3.6 – 4.2 eV) for all applied pressures, clearly indicating that the system operates in a non-thermal plasma regime in all cases [34]. This was also previously observed by Heijkers et al. for CO_2 conversion under NPD discharges [32].

3.3. *Modelled analysis of gas phase kinetics*

(a) **Electrons**

The temporal profile of electron density, showing pulsed behaviour in the model, is shown in Fig. 7a.

The calculated peak electron densities (*i.e.* during the pulses) vary

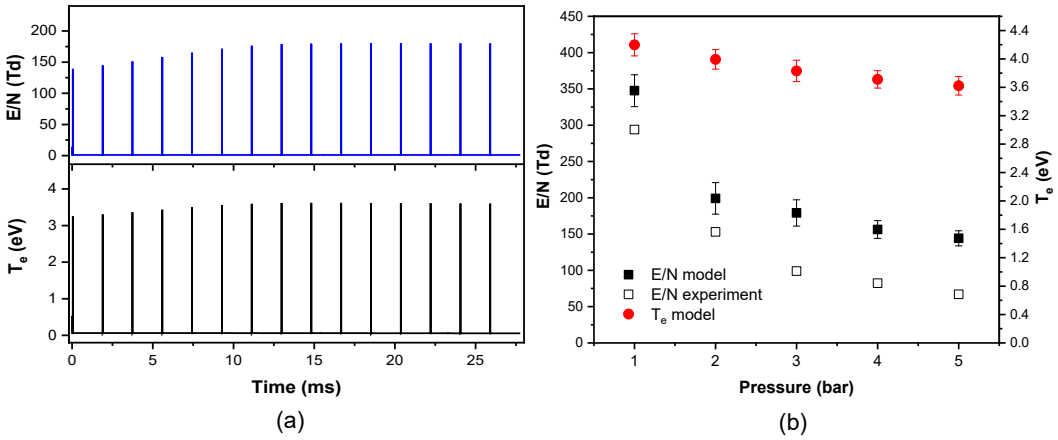

Fig. 5. (a) Calculated temporal profile of the reduced electric field (top) showing peaks which are coincidental to the power pulses, as well as pulsed behaviour of the calculated electron temperature as a response to the electric field (bottom). Both calculations were carried out at 4 bar. (b) Maximum reduced electric field and electron temperature values calculated by the model at different applied pressures. The experimental E/N is also shown for comparison.

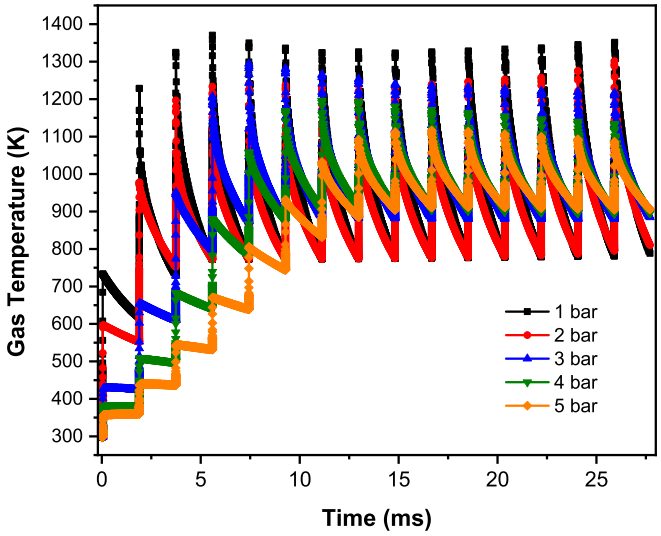

Fig. 6. Calculated temperature profiles at different applied pressures showing the pulsed evolution of calculated gas temperature within the gas residence time.

from 6.9×10^{15} cm^{-3} (at 5 bar) to 1.1×10^{16} cm^{-3} (at 1 bar) and this range agrees well with experimental data reported by Maqueo et al. [35] for CH_4 and CH_4/O_2 mixtures (*i.e.* order of 10^{15} to 10^{17} cm^{-3}). Consistent with other reports in literature, the electron density magnitude is inversely proportional to the applied pressure (Table 3) [13,18,35].

The electron density along the residence time reaches its peak at the top of each pulse (Fig. 7a). Though these densities are high (in line with the intense power discharges), they are very short lived and only last for 9 – 18 ns, depending on the pressure. Both electron density and electron temperature plummet to negligible values (~5×10^8 cm^{-3}) in the afterglow (in between the pulses), slowing down or halting electron impact processes, as recombination reactions become more important. The increase in the peak of electron density over the first 6 pulses (~10 ms) is related to the rise in the gas temperature in the same time period (green profile in Fig. 6). Due to the ideal gas law, this rise in the gas temperature decreases the number of species (density) in the gas phase,

Table 3
Maximum electron density at each applied pressure.

Pressure (bar)	Electron density (cm^{-3})
1	1.08×10^{16}
2	9.97×10^{15}
3	9.22×10^{15}
4	7.99×10^{15}
5	6.95×10^{15}

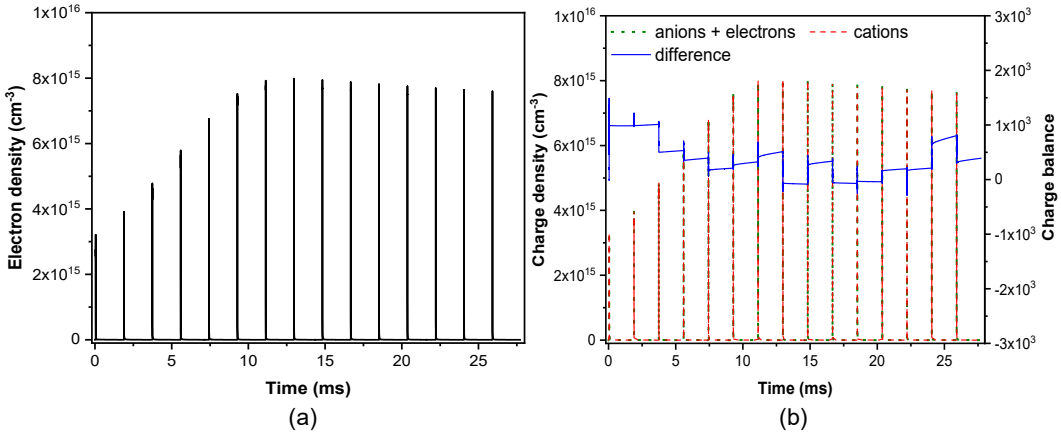

Fig. 7. Simulated profiles of (a) electron density and (b) sum of electrons and anions versus sum of cations (left y-axis), with the numerical difference shown on the right y-axis. These calculations were performed at 4 bar.

whilst pressure and volume are held constant. Since, the reduced electric field is inversely proportional to the density of neutral gas species, a reduction in the latter causes the reduced electric field to increase, leading to a proportional increase in electron density.

As shown in Fig. 7b, there is a precise overlay in the profiles of positive ions and of electrons plus negative ions, indicating a tight charge balance is kept throughout the simulations. The maximum difference observed (~10^3 cm^{-3}; right y-axis of Fig. 7b) lies within the error range of the model and is insignificant compared to the magnitude of the charge densities in the model (10^{11} – 10^{16} cm^{-3}).

(b) Feed gas molecules and major products

Fig. 8 displays density profiles of various important species considered in the model. It is clear that all profiles exhibit pulsed behaviour, where sharp and rapid decreases (for the gas feed molecules: CH_4 and H_2) and increases (for the radical and ionic species) occur in simultaneity with the power pulses, while much slower and gradual variations take place in the interpulse periods.

The reactants' profiles show (i) sudden drops where the pulses occur (especially within the first 10 ms of the simulations) and (ii) steady growth in the afterglow, signalling consumption and reformation, respectively (Fig. 8a). CH_4 and H_2 are chiefly decomposed through electron impact reactions during the power discharges, and reformed otherwise via the very efficient recombination channels of $CH_3 + H$ and $H + H$, respectively. Concomitantly, other recombination reactions lead to the formation of higher hydrocarbons. Overall, H_2 is consumed in the beginning, however production surpasses consumption after 11 pulses, and H_2 becomes thus a product of CH_4 conversion. Conversely, CH_4 exhibits a decreasing tendency throughout.

At 4 bar, C_2H_4 appears as the top product, followed by C_2H_2 and finally C_2H_6, which is a minor product in the entire pressure range. These C_2 species also undergo consumption by electron impact reactions during the pulses and are reformed in the afterglows, when electron density decreases between the pulses. After 8 ms, C_2H_4 becomes the dominant product and the density variations no longer affect the selectivity order at 4 bar (*i.e.* $C_2H_4 > C_2H_2 > C_2H_6$). It is of note that this onset accompanies the stabilisation of the gas temperature variation (see Fig. 6). While the steady state tendencies observed for the C_2H_4 and C_2H_6 products are roughly attained at 18 ms, the C_2H_2 density continues to increase slightly in the residence time.

To elaborate further on this analysis, the thermodynamic equilibrium compositions of the plasma reactor effluent over the operating temperature (750 – 1400 K, see Fig. 6) and pressure range of interest (1 – 5 bar) are presented in Fig. 9. When operating at atmospheric pressure and temperatures > 1200 K, C_2H_2 is the most stable, thereby, the most favourable product among the C_2 species. When operating at elevated pressures, particularly > 3 bar, C_2H_4 becomes the most favourable product over the discussed temperature range (750 – 1400 K). This behaviour tallies very well with the species density trends depicted in Fig. 8, as they match the equilibrium compositions shown in Fig. 9 (plot of 4 bar), suggesting that the rates of interconversion between C_2H_2 and C_2H_4 via other intermediate species are fast, thus, the relative C_2 concentrations can reach their thermodynamic equilibrium values. Among all the species, CH_4 appears to be the most stable, thereby, the most abundant species under the tested conditions.

In Section 3.5 we present a detailed analysis of the effect of pressure and temperature on the reaction pathways and in turn on the product

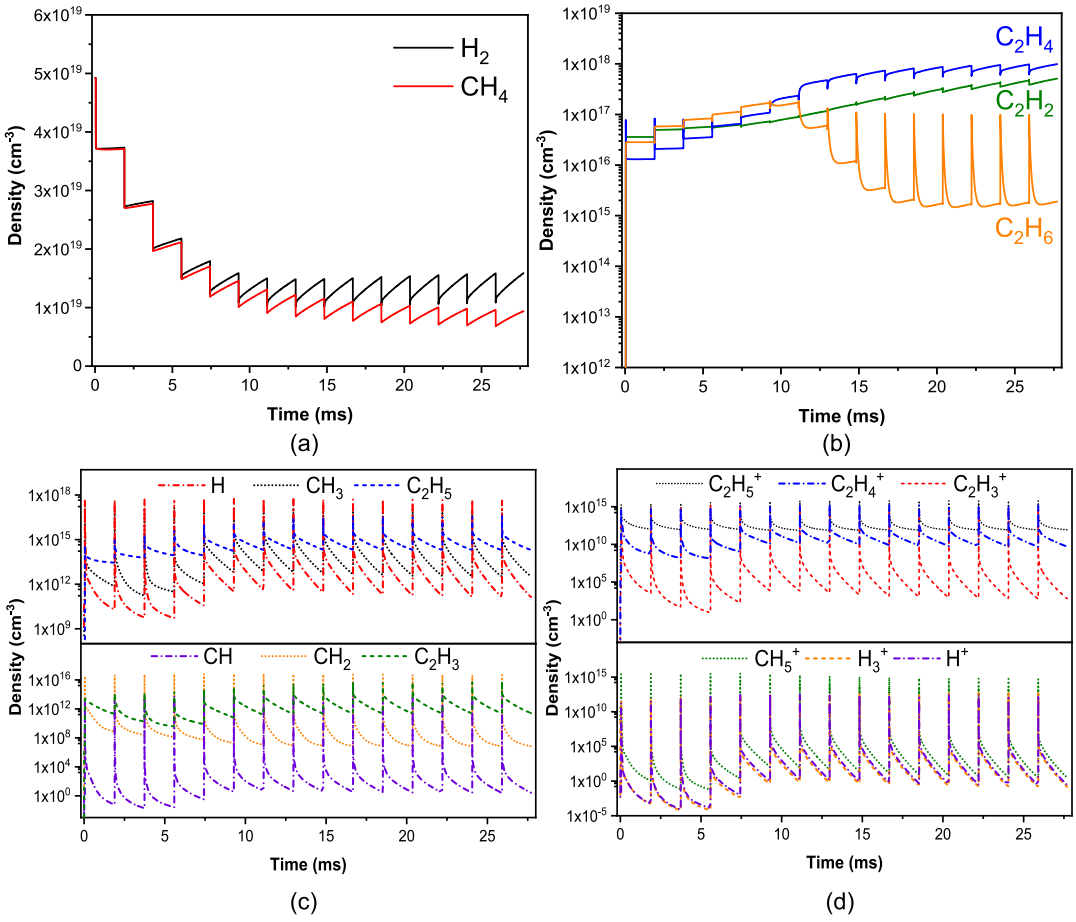

Fig. 8. Calculated density profiles of (a) feed gas molecules, (b) major products from non-oxidative CH_4 conversion, (c) most important radicals and (d) main cations in the simulations. These calculations were performed at an applied pressure of 4 bar.

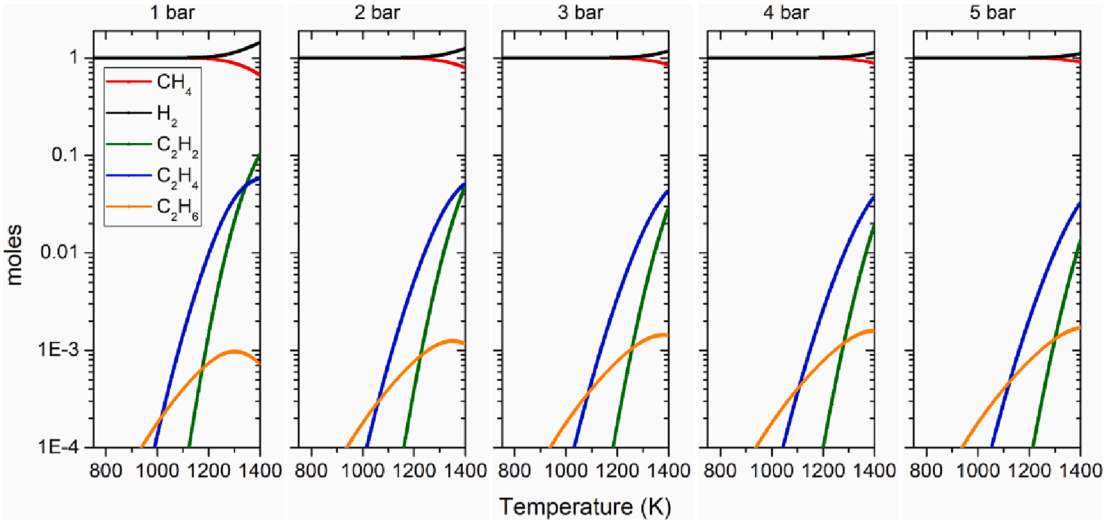

Fig. 9. Thermodynamic equilibrium compositions of the plasma reactor effluent over the operating temperature and pressure range of interest. The calculations were performed in ASPEN Plus process simulator, using the Peng-Robinson equation of state. Feed composition: CH_4:H_2 = 1:1.

selectivity.

(c) Radicals and ions

The calculated densities of the main radicals and ions are plotted in Fig. 8c and 8d, respectively. The densities of all other radicals and ions considered in the model were considerably lower, and therefore not included in this figure. The order of abundance of the radicals shown in the graphs is H > CH_3 > C_2H_5 > C_2H_3 > CH_2 > CH. The peak density for all radicals is suddenly (ns scale) reached through electron impact dissociation of molecules during the power pulses. In the wake of each pulse, the radical densities decrease sharply (falling to ~ 2/3 of the maximum density in the pulse) within 120 ns due to radical recombination. This decreasing tendency remains in later stages of the afterglow, up to the next pulse. However, it deaccelerates significantly, giving rise to the tails seen in the interpulse periods.

In Fig. 8d it is evident that the main ions in the model follow accurately the trends described above for the radicals. Electron impact ionisation and ionic recombination reactions account for peak cation production and consumption, respectively. The order of abundance of the ions is as follows: $C_2H_5^+$ > $C_2H_4^+$ > H^+ > $C_2H_3^+$ > CH_5^+ > H_3^+.

3.4. Calculated conversion and selectivity, and validation with experiments

The calculated and experimental results for CH_4 conversion and C_2 products selectivity are plotted and compared in Fig. 10.

As observed in Fig. 10, it is evident that pressure plays a major role for both conversion and selectivity in the non-oxidative CH_4 coupling. In terms of conversion, both model and experiments show that pressure increase has a beneficial effect up to ~ 4 bar (in the experiments; ~ 3 bar in the model), however a further increase to 5 bar leads to lower conversion than those registered at 3 and 4 bar.

Selectivity varies widely across the pressure range under study. At 1 bar, C_2H_2 is clearly the major product (at ~ 60%, both in the model and the experiments), followed by C_2H_4 (at 10% in the experiments and 20% in the model) and finally C_2H_6 appearing as a minor product in the reaction (at ~ 5%, both the experiments and the model). Such observations for product distribution at 1 bar are in line with other studies of CH_4 conversion under NPD [13,33]. Raising the pressure to 2 bar causes significant enhancement in C_2H_4 production and reduces C_2H_2 formation, resulting in higher selectivity towards C_2H_4 than C_2H_2 in the experiments. In the model, though C_2H_2 still shows marginally leading

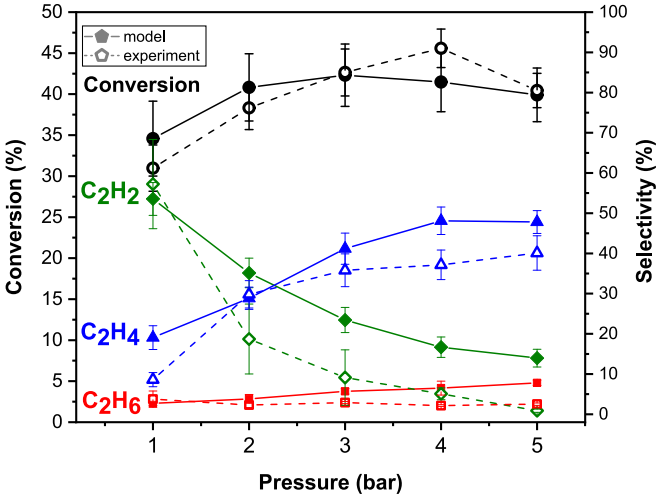

Fig. 10. CH_4 conversion and selectivity of C_2H_6, C_2H_4 and C_2H_2. Modelled and experimental results are compared across the 1 to 5 bar pressure range.

selectivity at 2 bar, the trend of rising C_2H_4 formation is accurately captured. In both model and experiment, from 3 to 5 bar, C_2H_4 becomes the dominant product, and its selectivity continues to increase, whilst the C_2H_2 selectivity dwindles with every pressure increment. In fact, the C_2H_2 selectivity falls to ~ 5% at 4 bar and ~ 1% at 5 bar in the experiments, while remaining at ~ 15% in the model (the reason for this contrast is explained below). Nevertheless, the decaying trend is qualitatively captured by the model. Though the model predicts a gradual increase in C_2H_6 selectivity with pressure (peaking at ~ 8% at 5 bar), this is not backed up by the experiment, showing that C_2H_6 production is not affected by the applied pressure and remains very slow in all cases.

The model predicts production of appreciable quantities of C_3H_6 and C_3H_8, with maximum selectivity (at 5 bar) of 4% and 5.5%, respectively. In the model, C_3H_6 and C_3H_8 are formed at all pressures and their selectivity rises as the pressure is increased. Since C_3 products (or higher hydrocarbons) were not measured in the experiments, this prediction cannot be validated by experimental data. Formation of C_3H_6, C_3H_8 and $C_{(s)}$ (discussed below) is most likely the reason for the less than 100% selectivity observed in the model and experiments.

Significant amounts of coking, *i.e.*, $C_{(s)}$, are produced in the experiments, but remained unquantified. This is likely one of the main reasons,

along with C_2H_2 into C_2H_4 hydrogenation promoted by the copper-based HV electrode, for the overestimation in the production of all C_2 products in the model, leading to higher C_2 selectivity compared to experimental values, especially at higher pressures. Though low quantities of $C_{(s)}$ are calculated in the model, extensive formation of solid carbon is observed in the reactor and this is detrimental to C coupling into higher hydrocarbons, in turn reducing C_2 selectivity. We believe the model calculations under predicts the formation of $C_{(s)}$, which in turn overestimates the production (and selectivity) of other products. Indeed, stepwise gas-phase dehydrogenation of C_2H_2 into $C_{(s)}$ is the only route considered in the model. In future works, we plan to study the potential C_2H_2 hydrogenation into C_2H_4 catalysed by the copper-based HV electrode in the NPD plasma experiments (as previously discussed in the reactor performance analysis, see Section 3.1) [31,36,37] and to include more surface species and decomposition reactions, such as benzene pyrolysis and dehydrogenation reactions at the reactor walls (main production avenues for carbon particles) [6,38,39]. However, this lies outside the scope of the present study, among other reasons, because it would require unreasonable computational resources.

In summary, modelled and experimental results correspond well for (i) absolute values (maximum 12% discrepancy for C_2H_2 selectivity at 5 bar) and (ii) trends across the pressure range. Therefore, in the coming section we will use the model to perform reaction pathway and mechanism analyses and draw correlations between pressure, temperature and gas-phase reactivity.

3.5. Reaction pathway analysis

The formation and consumption routes of various species were investigated using time-resolved calculations of reaction rates (in the pulses and in the afterglows) of all processes included in the model. We assessed the reactivity of the multitude of species in the plasma system at steady state and composed an integral reaction pathway diagram for the reactants and most abundant products in the model. This reaction pathway analysis was carried out for all pressures, offering insights into the interplay between pressure, temperature and reactivity of ions and molecules and the overall selectivity. The findings are discussed below and presented in Fig. 11 (which shows all major neutral reaction pathways), 12 and 13.

CH_4, methane: As feed gas molecule, methane is one of the most abundant species in the model. As the electron density peaks on the timescale of the pulses, methane is converted into vibrationally excited CH_4 (v1, 3) (exclusively via electron collisions) and CH_4 (v2, 4) (via electron collisions and so-called vibrational-vibrational (VV) relaxation from the CH_4 (v1, 3) states), and also into electronically excited CH_4* (at 7.9 eV), by electron impact excitation. As soon as the electron density drops in the very early afterglow (nanosecond scale after the pulse), over 99.95% of the vibrationally excited CH_4 species undergo deexcitation, returning to ground state CH_4 via the so-called vibrational-translational (VT) relaxation. Therefore, under the simulated conditions and timescale considered, our model confirms that the vibrational excitation channel does not drive dissociation of CH_4. This result is in line with previous observations described in studies by Heijkers *et al.*, [28] Butterworth *et al.* [40] and Maitre *et al.* [41]. Thus, for clarity, the vibrationally (and also electronically) excited CH_4 molecules are not shown in Figs. 11 and 13.

CH_4 dissociation is initiated by electron impact reactions within the power pulse, leading to CH_3 (89.1%), CH_2 (4.76%) and CH (0.45%) radicals. This is illustrated in Fig. 8c where radical densities are observed peaking with each pulse. The vast majority of C_1 radicals are generated from ground state CH_4 and from CH_4* (7.9 eV). Especially in the case of CH_3 radicals, CH_4 and CH_4* (7.9 eV) are the main sources, with contributions of 11.90% and 84.35%, respectively. As the afterglow of each pulse begins and electron density drops, radical recombination reactions gain extensive traction, generating higher hydrocarbons (discussed below) and reforming H_2 and CH_4. Two reformation reactions that should be underlined are (i) $H + H + M \rightarrow H_2 + M$, accounting for 15% of the H radical total consumption and

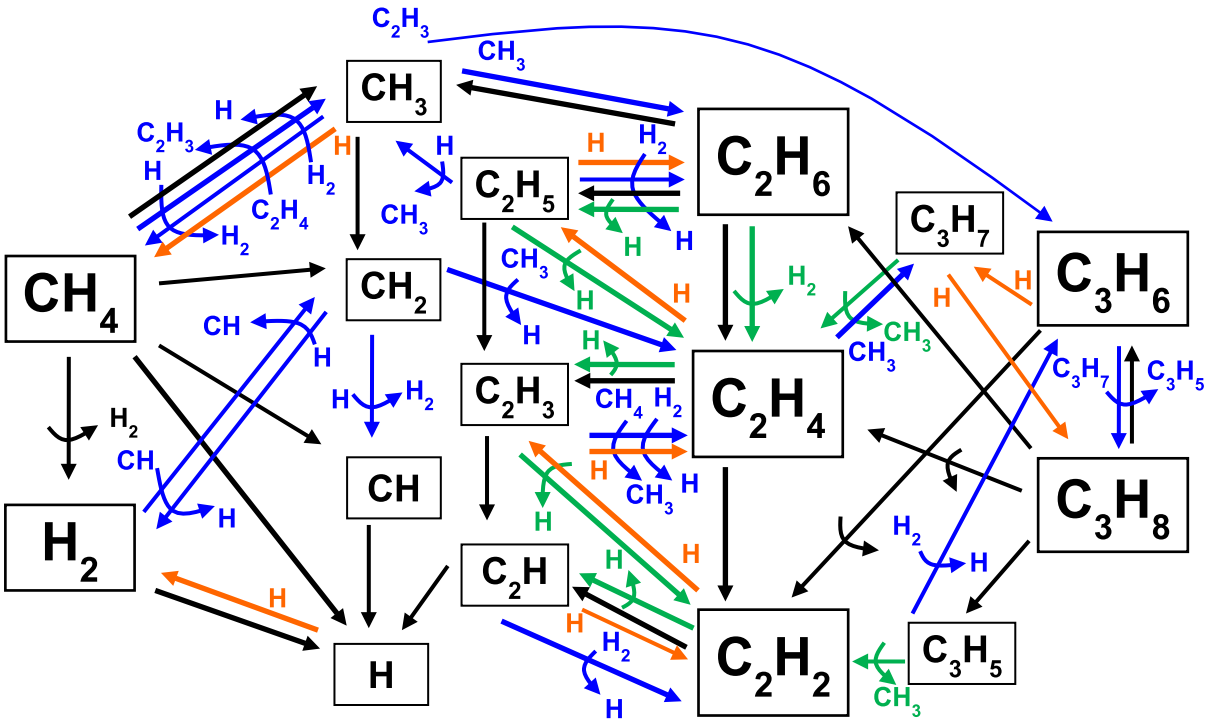

Fig. 11. The complex network of species and reactions involved in (50%) CH_4 and (50%) H_2 conversion at steady state (this analysis was performed at 4 bar). Thicker arrows in the diagram indicate important reactions listed in the discussion section. Black arrows indicate electron impact dissociation, blue arrows indicate recombination reactions, except H radical addition reactions which are the most abundant type of reaction between neutral species and therefore indicated by orange arrows for clarity. Finally, green arrows indicate decomposition reactions. Reactants and products are also shown alongside the arrows.

contributing with 34% to H_2 production, as well as (ii) $CH_3 + H + M \rightarrow CH_4 + M$, accounting for 18% and 13% of CH_3 and H radical total consumption, respectively, and being responsible for 78% of CH_4 reformation. These values apply to the 1 bar case and the percentages rise upon pressure increase.

H_2, hydrogen: H_2 also has high initial density and also undergoes a vibrational excitation-deexcitation loop, very similar to that discussed above for CH_4. Upon start of the pulses, ground state H_2 molecules are excited to H_2 (v1 – 14) and rapidly deexcited, returning to ground state H_2 via VT relaxation. While the relaxation of vibrationally excited H_2 levels is crucial for gas-phase heating, H_2 (v1 – 14) molecules, just as CH_4 (v1 – 4), do not enter dissociation channels to any appreciable extent. Dissociation into H radicals takes place from ground state H_2 (99%) passing through the electronically excited state H_2* (11.83 eV) which, in the model, is a lump of four electronically excited states of H_2: $H_2(b^3\Sigma_u^+)$, $H_2(b^1\Sigma_u^+)$, $H_2(c^3\Pi_u^+)$ and $H_2(a^3\Sigma_g^+)$. H radicals are chiefly produced by H_2 dissociation with 47% contribution, while $CH_4 + e^- \rightarrow CH_3 + H$ is the second most important channel in H radical production with 20% contribution. H radicals are the single most important radicals in the system, as they participate in all hydrogenation reactions and are involved in H_2 and CH_4 reformation.

A reaction pathway diagram displaying a complex network with the main processes for dissociation and recombination of the most important molecules and radicals in the system is shown in Fig. 11. The pathways considered above, and the reactions involved in the formation of C_2 and C_3 products are shown in the context of the entire reaction set. In Fig. 12 (below), the separate production processes for the C_2 hydrocarbons are indicated in more detail, along with tables for their relative contributions at the different pressures investigated.

C_2H_2, acetylene: C_2H_2 is the least hydrogenated species amongst the

(a)

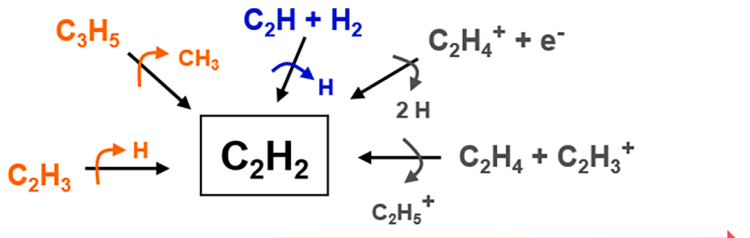

	1 bar	2 bar	3 bar	4 bar	5 bar
C_2H_3 dehydrogenation (%)	56	51	50	49	38
C_3H_5 demethylation (%)	10	14	14	15	11
$C_2H + H_2$ recombination (%)	32	22	6		
Charge transfer / ion dissociation (%)		3	16	18	25

(b)

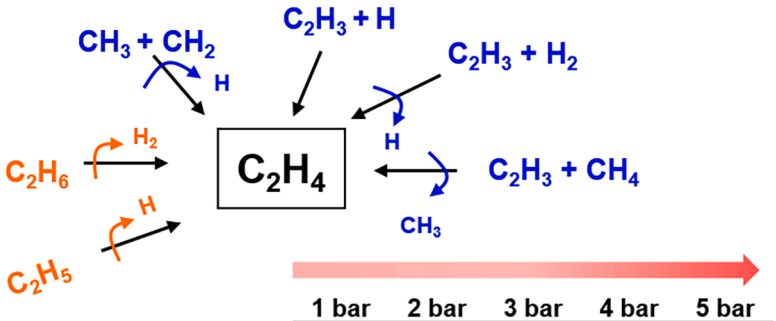

	1 bar	2 bar	3 bar	4 bar	5 bar
C_2H_3 + H recombination (%)		8	26	37	43
C_2H_3 + (H_2 & CH_4) recombination (%)	20	18	19	20	19
$CH_3 + CH_2$ recombination (%)	9	10	8	9	7
C_2H_5 / C_2H_6 dehydrogenation (%)	65	60	41	29	26

(c)

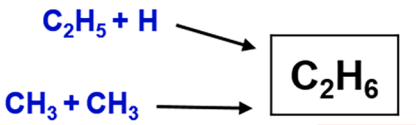

	1 bar	2 bar	3 bar	4 bar	5 bar
$CH_3 + CH_3$ recombination (%)	62	65	66	71	74
C_2H_5 + H recombination (%)	29	29	33	20	19

Fig. 12. Principal reaction pathways leading to formation of (a) C_2H_2, (b) C_2H_4 and (c) C_2H_6 hydrocarbons in our model. The contribution (%) of each formation route is given across the studied pressure range.

stable C_2 hydrocarbons. It is mostly produced via dehydrogenation of C_2H_3 (which is in turn chiefly formed via stepwise dehydrogenation of C_2H_4, C_2H_5 and C_2H_6) and by C_2H and H_2 recombination reactions. In line with our previous mechanistic report [11,18], our model confirms stepwise dehydrogenation is the primary route for C_2H_2 production at 1 bar and also stands as the main route across the entire pressure range (see Table in Fig. 12a). The efficiency remains approximately constant from 1 to 4 bar and declines at 5 bar. Also, demethylation of C_3H_5 is non-negligible to C_2H_2 production, and alongside C_2H_3 dehydrogenation, these dissociations are the main production channel in the entire pressure range. The recombination between C_2H and H_2 is important at 1 bar, but loses efficiency at 2 bar and becomes insignificant above 3 bar (see Table in Fig. 12a). At higher pressures (>4 bar), as the two main production channels lose strength, the ionic reactions (also shown in Fig. 12a) start to play a role in C_2H_2 formation.

C_2H_2 undergoes decomposition whilst the power pulses are discharged and in the early afterglow, about ~ 120 ns after each power pulse (as the gas temperature peaks). The larger fraction (57%) of C_2H_2 conversion takes place through dehydrogenation upon electron collision:

$$e^- + C_2H_2 \rightarrow C_2H + H + e^-$$

Besides, hydrogenation of C_2H_2 into C_2H_3 as well as C_2H_2 dissociation upon collision with any neutral molecule (M) account for 22% and 10% of its total consumption, respectively:

$$C_2H_2 + H + M \rightarrow C_2H_3 + M$$

$$C_2H_2 + M \rightarrow C_2H + H + M$$

Once created, C_2H radicals mostly hydrogenate and return to C_2H_2 but also form C_2H_3 and C_2H_5 radicals (not indicated in Fig. 11, for the sake of clarity). C_2H_3 radicals undergo both hydrogenation (leading to C_2H_4 and eventually C_2H_6) and dehydrogenation (reforming C_2H_2).

Considering these pathways, C_2H_2 essentially seems to cycle through dehydrogenation and re-hydrogenation processes with high production efficiency, especially at lower pressures. While the former process leads to C_2H (and C_2H_2 from C_2H_3) and occurs during the power peaks when electrons have maximum energy, the latter takes place immediately after the pulse mainly at 1 bar.

C_2H_4, ethylene: Similar to C_2H_2, hydrogenation and dehydrogenation reactions are the principal channel for C_2H_4 formation, as displayed in Figs. 11 and 12b. At low pressures (1 and 2 bar), dehydrogenation of C_2H_5 and C_2H_6 provides the largest contribution towards C_2H_4 formation [33,42]. However, the efficiency of these dehydrogenations dwindles as the pressure is increased (see table in Fig. 12b), highlighting the negative effect of high pressure on decomposition reactions. On the other hand, hydrogenation of C_2H_3 (*i.e.* C_2H_3 + H recombination) accounts for the majority of C_2H_4 production in the high-pressure range (3 to 5 bar), and becomes the dominant process at 4 and 5 bar (see table in Fig. 12b). The C_2H_3 + H_2 or CH_4 recombination reactions are also important, as well as CH_3 + CH_2 recombination, but do not depend on the applied pressure, thus their contribution remains constant across the range. Considering that C_2H_3 is the most abundant C_2 radical, it is not surprising that the main pathways for C_2H_4 formation involve this species.

Conversion of C_2H_4 takes place through three distinct channels: (i) hydrogenation to C_2H_5 and (ii) methylation to C_3H_7 both in the late afterglow and (iii) electron impact dissociation to C_2H_3 and C_2H_2 during the power peaks, and these account for 74%, 6% and 19% of the total C_2H_4 consumption, respectively. Like C_2H_2, C_2H_4 and C_2H_3 undergo cycles of hydrogenation, dehydrogenation and re-hydrogenation.

From the C_2H_2 and C_2H_4 formation and destruction pathway analysis, we can deduce that at low pressures the production of C_2H_2 is favoured, since the dehydrogenation of C_2H_3 (*i.e.* decomposition of C_2H_3 into C_2H_2 and H) is a very efficient channel (see Table in Fig. 12a). From 3 bar to 5 bar, the principal channel for C_2H_3 conversion shifts from dehydrogenation to C_2H_2 into re-hydrogenation to C_2H_4. In fact, hydrogenation of C_2H_3 (with H radicals, and also with H abstraction from H_2 and CH_4 molecules) becomes the most effective avenue for C_2H_4 production (see Table in Fig. 12b), boosting its yield and growing as the main product of CH_4 conversion.

C_2H_6, ethane: Unlike C_2H_2 and C_2H_4, gain and loss of H radicals are not the main avenue for C_2H_6 production. C_2H_6 is chiefly formed via recombination between CH_3 radicals and the effectiveness of this route increases with pressure (see Table in Fig. 12c). It is interesting to note that in the overall process of CH_4 coupling, C_2H_6 is the first C_2 species to be produced (see initial 5 pulses in Fig. 8b) owing to the much higher density of CH_3 radicals compared to other C_1 radicals. C_2H_6 is decomposed via three electron impact dissociation reactions, accounting for 45%, 36% and 10% of C_2H_6 consumption, respectively:

$$C_2H_6 + e^- \rightarrow C_2H_4 + H_2 + e^-$$

$$C_2H_6 + e^- \rightarrow C_2H_5 + H + e^-$$

$$C_2H_6 + e^- \rightarrow CH_3 + CH_3 + e^-$$

Also, as the gas temperature rises and stabilises in steady state, C_2H_6 undergoes decomposition into C_2H_4 and C_2H_5 via dehydrogenation (green arrows in Fig. 11). These new C_2 products will recombine and further dissociate, eventually entering a cycle leading to steady production of C_2H_4 and C_2H_2 as the main products observed at each studied pressure.

At all pressures, the gas temperature in the plasma zone is much too high for selective C_2H_6 production, and therefore it is obvious that this product's selectivity remains very low across the entire pressure range.

Ions: The ions are not included in Figs. 11 and 12 above, as they do not play a dominant role in the reaction scheme. However, to highlight their importance in the chemistry, the principal positive ions along with their formation and destruction routes are shown in Fig. 13 below.

Positive ions are exclusively produced through electron impact reactions, as soon as the first pulse is discharged, either via direct ionisation or dissociative ionisation. The three most abundant ions primarily formed from the reactants in the feed gas are H^+, CH_4^+ and CH_3^+, and subsequently these positive ions react with neutral molecules (via H^+ abstraction and electron transfer processes), creating secondary ions (see Fig. 13). The most important secondary positive ions are H_3^+, CH_5^+, $C_2H_5^+$ and $C_2H_3^+$. $C_2H_3^+$ and $C_2H_5^+$ are also produced via electron impact ionisation from their neutral counterparts, while H_3^+, CH_5^+ are exclusively formed via recombination reactions from the primary ions.

Besides their fundamental role in keeping the charge balance in a plasma environment, this reaction pathway analysis reveals the important role of ions and their reactions in the reformation of H_2 and the production of C_2H_2. Some of the main neutralisation avenues for H_3^+, CH_5^+, $C_2H_5^+$ and $C_2H_3^+$ (especially dissociative neutralisation reactions) result in creation of H_2 and C_2H_2 molecules, as shown in Fig. 13.

3.6. Heating and cooling mechanisms

As the gas temperature dynamics (*i.e.*, heating and cooling during and after the pulses) play a crucial role in the chemistry of NPD, we also used our model calculations and simulated temperature profiles to perform heat transfer analyses and garner quantitative information on individual reaction contributions to heating and cooling at steady state conditions. In Fig. 14, we plot the gas temperature (red curve) and the reduced electric field (E/N) (blue curve, to indicate the pulses), for (a) one pulse and the beginning of the ensuing afterglow and (b) two consecutive pulses and afterglows, emphasising the late afterglow periods. The gas temperature undergoes a sharp increase in the model following the E/N peak within the power discharges, as shown in Fig. 14a.

This temperature rise is due to heat release through exothermic

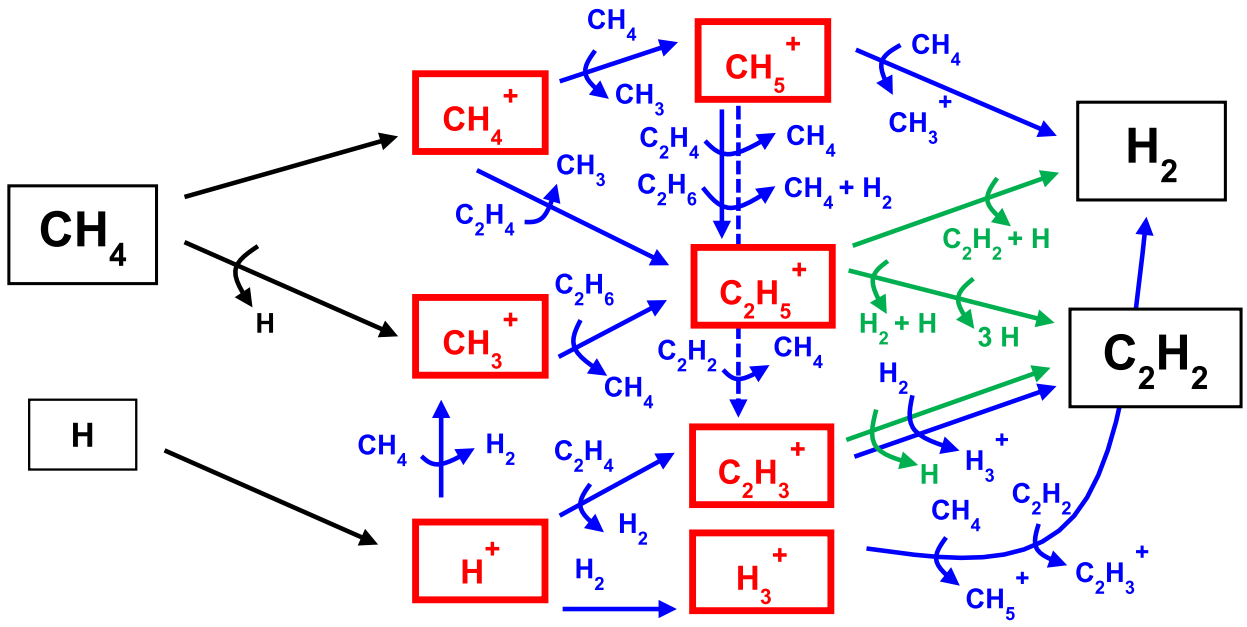

Fig. 13. Network of reactions and species involved in the formation and consumption of important ions in the model. This figure highlights the role of ionic processes in the synthesis of C_2H_2 (especially at high pressures) and reformation of H_2. Black arrows indicate electron impact ionisations, blue arrows indicate recombination reactions and green arrows indicate dissociative neutralisation reactions.

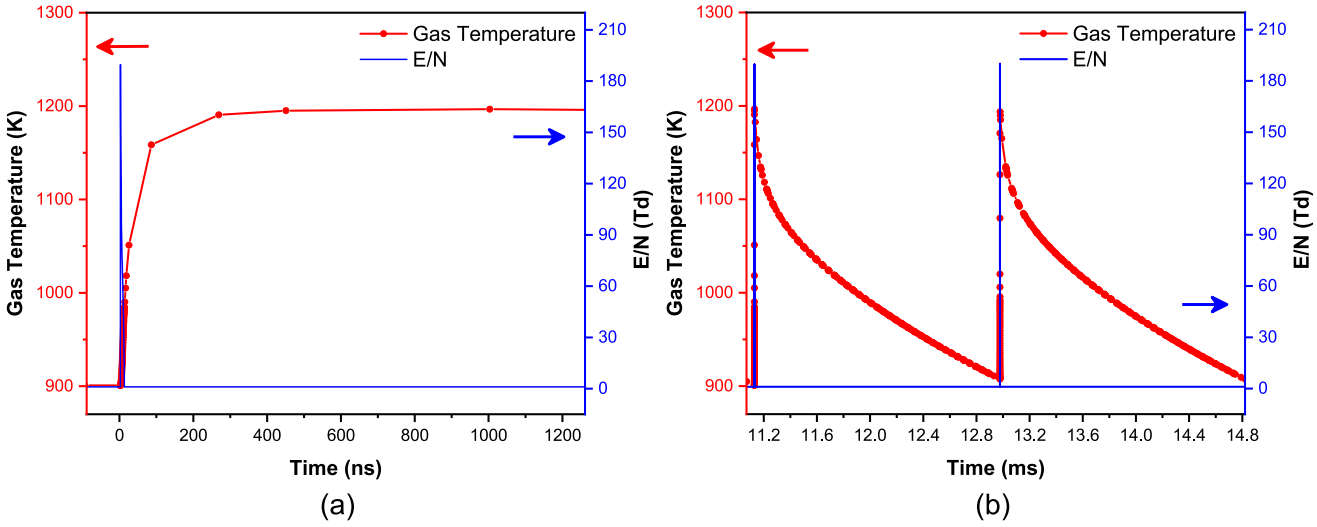

Fig. 14. E/N (blue) and gas temperature (red) profiles over (a) one power pulse and beginning of the ensuing afterglow (the relative scale of the x-axis was adjusted for pulse start at t = 0 ns) and (b) two consecutive pulses and two complete afterglows. This calculation was carried out at 4 bar.

processes and occurs on a similar timescale (ns scale) to that of the pulses. The mechanism for heat release in the system can be understood in three parts.

(i) As the electron density peaks in the pulses, the rate of elastic momentum transfers is the highest, leading to heating of the gas phase.
(ii) Also in the pulse, H_2 vibrational levels are rapidly populated and resulting relaxation (through VT processes) releases heat to the gas phase. These two events cause the steep temperature rise seen in Fig. 14a and account for 34% and 29% of the total heating, respectively.
(iii) In the early afterglow, *i.e.* 500 ns after the electron density drops, the exothermic recombination reaction, $CH_3 + H + M \rightarrow CH_4 + M + \Delta H$, sustains the temperature rise on the μs scale (see also Fig. 14a), while the cooling events are activated. H and CH_3 radical recombination is responsible for 35% of the total heat release in the model.

Conversely, cooling is a much slower process, as it takes place steadily throughout the afterglow, giving rise to the sawtooth profile (red curve in Fig. 14b). Heat loss to the reactor walls is the principal cooling event in the system with a contribution of 76% to the total heat loss. Noticeably, cooling is more pronounced in the early afterglow. This is due to two endothermic reactions which take place at high rates in that interval: $C_2H_5 + M + \Delta H \rightarrow C_2H_4 + H + M$ (11 – 17%) and $C_2H_3 + M + \Delta H \rightarrow C_2H_2 + H + M$ (8 – 14%). In the late afterglow, these two reactions lose importance, as stable molecules are formed and the density of radicals drops.

Upon rising pressure, the E/N peaks drop (see Fig. 5b), lowering the rate of energy transfer from electrons to the gas-phase molecules via elastic collisions and vibrational relaxation. Thus, the temperature peaks

become less accentuated at higher pressures. Moreover, at high pressures, endothermic dissociations (such as the C_2H_3 and C_2H_5 decompositions mentioned above) also have significantly lower rates (since maintenance of fewer molecules is favoured), slowing the overall cooling process in the afterglow. Combined, these two effects play a role in progressively reducing the amplitude between the maximum temperature following the pulses and the minimum temperature at the end of each afterglow, as was observed in Fig. 6 above.

4. Conclusions

In this work, nanosecond pulsed discharges have been studied for methane conversion using a 0D plasma kinetic model, and validated against an experimental setup showing good alignment for conversion and products selectivity. Experimental power deposition characteristics from a coaxial plasma reactor over a pressure range of 1 to 5 bar were taken as input in a 0D model that performs self-consistent gas temperature calculations and incorporates gas temperature and pressure dependent reaction rates.

The simulation results highlight pulsed behaviour in all the physical parameters, such as electric field, gas temperature and electron energy, and the densities of plasma species also exhibit pulsed profiles. Good agreement was observed with the experimental measurements of CH_4 conversion and C_2 hydrocarbon selectivity, which indicates that the gas-phase kinetic dynamics occurring in the reactor are comparable to those included in the model. A reaction pathway analysis of the simulation results demonstrates that the mechanisms responsible for formation of different C_2 products change upon increasing pressure of the system, which is of importance when considering the C_2H_2 and C_2H_4 selectivity trends in the 1 to 5 bar pressure range. Further analysis of the processes that lead to temperature variations in the gas phase highlights the complexity of the interactions between the different plasma species in such a system.

In our future work we plan to look at the effect of carbon deposition and the influence of surfaces on the resulting products and selectivity, with main focus on how post-plasma catalysts can improve the ethylene selectivity by hydrogenation from acetylene. Indeed, the conversion of methane into ethylene using nanosecond pulsed discharges with post-plasma catalysis remains a complex process that requires further study.

Declaration of Competing Interest

The authors declare that they have no known competing financial interests or personal relationships that could have appeared to influence the work reported in this paper.

Data availability

Data will be made available on request.

Acknowledgments

We gratefully acknowledge financial support by the Flemish Government through the Moonshot cSBO project “Power-to-Olefins” (P2O; HBC.2020.2620).

Appendix A. Supplementary data

Supplementary data to this article can be found online at https://doi.org/10.1016/j.cej.2023.142227.

References

[1] J.R. Fincke, R.P. Anderson, T.A. Hyde, B.A. Detering, Plasma pyrolysis of methane to hydrogen and carbon black, Ind. Eng. Chem. Res. 41 (2002) 1425–1435.
[2] J.R. Fincke, et al., Plasma Thermal Conversion of Methane to Acetylene, Plasma Chem. Plasma Process. 22 (2002) 105–136.
[3] X. Guo, et al., Direct, nonoxidative conversion of methane to ethylene, aromatics, and hydrogen, Science (80-.) 344 (2014) 616–619.
[4] M. Scapinello, E. Delikonstantis, G.D. Stefanidis, The panorama of plasma-assisted non-oxidative methane reforming, Chem. Eng. Process. 117 (2017) 120–140.
[5] S.Y. Liu, D.H. Mei, Z. Shen, X. Tu, Nonoxidative conversion of methane in a dielectric barrier discharge reactor: Prediction of reaction performance based on neural network model, J. Phys. Chem. C 118 (2014) 10686–10693.
[6] N. García-Moncada, G. van Rooij, T. Cents, L. Lefferts, Catalyst-assisted DBD plasma for coupling of methane: Minimizing carbon-deposits by structured reactors, Catal. Today 369 (2021) 210–220.
[7] C. Shen, D. Sun, H. Yang, Methane coupling in microwave plasma under atmospheric pressure, J. Nat. Gas Chem. 20 (2011) 449–456.
[8] H. Shuanghui, et al., Conversion of methane to C_2 hydrocarbons and hydrogen using a gliding Arc reactor, Plasma Sci. Technol. 15 (2013) 555–561.
[9] Y. Yang, Methane conversion and reforming by nonthermal plasma on pins, Ind. Eng. Chem. Res. 41 (24) (2002) 5918–5926.
[10] D.L. Kuznetsov, V.V. Uvarin, I.E. Filatov, Plasma chemical conversion of methane by pulsed electron beams and non-self-sustained discharges, J. Phys. D. Appl. Phys. 54 (43) (2021) 435203.
[11] E. Delikonstantis, M. Scapinello, G.D. Stefanidis, Low energy cost conversion of methane to ethylene in a hybrid plasma-catalytic reactor system, Fuel Process. Technol. 176 (2018) 33–42.
[12] S.L. Yao, E. Suzuki, N. Meng, A. Nakayama, A High-Efficiency Reactor for the Pulsed Plasma Conversion of Methane, Plasma Chem. Plasma Process. 22 (2002) 225–237.
[13] R. Lotfalipour, A.M. Ghorbanzadeh, A. Mahdian, Methane conversion by repetitive nanosecond pulsed plasma, J. Phys. D. Appl. Phys. 47 (36) (2014) 365201.
[14] S. Zhang, et al., Time-resolved characteristics and chemical kinetics of non-oxidative methane conversion in repetitively pulsed dielectric barrier discharge plasmas, J. Phys. D. Appl. Phys. 51 (2018) 16.
[15] S. Kado, K. Urasaki, Y. Sekine, K. Fujimoto, T. Nozaki, K. Okazaki, Reaction mechanism of methane activation using non-equilibrium pulsed discharge at room temperature, Fuel 82 (18) (2003) 2291–2297.
[16] Y. Gao, et al., Highly efficient conversion of methane using microsecond and nanosecond pulsed spark discharges, Appl. Energy 226 (2018) 534–545.
[17] M. Scapinello, E. Delikonstantis, G.D. Stefanidis, Direct methane-to-ethylene conversion in a nanosecond pulsed discharge, Fuel 222 (2018) 705–710.
[18] M. Scapinello, E. Delikonstantis, G.D. Stefanidis, A study on the reaction mechanism of non-oxidative methane coupling in a nanosecond pulsed discharge reactor using isotope analysis, Chem. Eng. J. 360 (2019) 64–74.
[19] E. Delikonstantis, M. Scapinello, O. Van Geenhoven, G.D. Stefanidis, Nanosecond pulsed discharge-driven non-oxidative methane coupling in a plate-to-plate electrode configuration plasma reactor, Chem. Eng. J. 380 (2020), 122477.
[20] M. Scapinello, L.M. Martini, G. Dilecce, P. Tosi, Conversion of CH_4/CO_2 by a nanosecond repetitively pulsed discharge, J. Phys. D. Appl. Phys. 49 (2016).
[21] K. Takashima (Udagawa), Y. Zuzeek, W.R. Lempert, I.V. Adamovich, Characterization of a surface dielectric barrier discharge plasma sustained by repetitive nanosecond pulses, Plasma Sources Sci. Technol. 20 (5) (2011) 055009.
[22] R. Lee, R. Labrecque, J.-M. Lavoie, Inline analysis of the dry reforming process through fourier transform infrared spectroscopy and use of nitrogen as an internal standard for online gas chromatography analysis, Energy Fuel 28 (12) (2014) 7398–7402.
[23] S. Pancheshnyi, B. Eismann, G. Hagelaar, L. Pitchford, ZDPlasKin: a new tool for plasmachemical simulations. in *American Physical Society, 61st Annual Gaseous Electronics Conference*, 2008.
[24] G.J.M. Hagelaar, L.C. Pitchford, Solving the Boltzmann equation to obtain electron transport coefficients and rate coefficients for fluid models, Plasma Sources Sci. Technol. 14 (2005) 722–733.
[25] T. Kozák, A. Bogaerts, Evaluation of the energy efficiency of CO_2 conversion in microwave discharges using a reaction kinetics model, Plasma Sources Sci. Technol. 24 (1) (2015) 015024.
[26] K. van ‘t Veer, F. Reniers, A. Bogaerts, Zero-dimensional modeling of unpacked and packed bed dielectric barrier discharges: The role of vibrational kinetics in ammonia synthesis, Plasma Sources Sci. Technol. 29 (4) (2020) 045020.
[27] Van 'T Veer, K., et al., Spatially and temporally non-uniform plasmas: Microdischarges from the perspective of molecules in a packed bed plasma reactor. *J. Phys. D*, Appl. Phys. 54 (2021) 15.
[28] S. Heijkers, M. Aghaei, A. Bogaerts, Plasma-Based CH_4 Conversion into Higher Hydrocarbons and H_2: Modeling to Reveal the Reaction Mechanisms of Different Plasma Sources, J. Phys. Chem. C 124 (2020) 7016–7030.
[29] A. Lo, A. Cessou, C. Lacour, B. Lecordier, P. Boubert, D.A. Xu, C.O. Laux, P. Vervisch, Streamer-to-spark transition initiated by a nanosecond overvoltage pulsed discharge in air, Plasma Sources Sci. Technol. 26 (4) (2017) 045012.
[30] A. Holmen, O. Olsvik, O.A. Rokstad, Pyrolysis of natural gas: chemistry and process concepts, Fuel Process. Technol. 42 (1995) 249–267.
[31] S. Wang, K. Uwakwe, L. Yu, J. Ye, Y. Zhu, J. Hu, R. Chen, Z. Zhang, Z. Zhou, J. Li, Z. Xie, D. Deng, Highly efficient ethylene production via electrocatalytic hydrogenation of acetylene under mild conditions, Nat. Commun. 12 (1) (2021).
[32] S. Heijkers, L.M. Martini, G. Dilecce, P. Tosi, A. Bogaerts, Nanosecond Pulsed Discharge for CO_2 Conversion: Kinetic Modeling to Elucidate the Chemistry and Improve the Performance, J. Phys. Chem. C 123 (2019) 12104–12116.
[33] S. Ravasio, C. Cavallotti, Analysis of reactivity and energy efficiency of methane conversion through non thermal plasmas, Chem. Eng. Sci. 84 (2012) 580–590.
[34] A. Fridman (Ed.), Plasma Chemistry, Cambridge University Press, 2008.

[35] P.D.G. Maqueo, M. Maier, M.D.G. Evans, S. Coulombe, J.M. Bergthorson, Regimes of an atmospheric pressure nanosecond repetitively pulsed discharge for methane partial oxidation, J. Phys. D. Appl. Phys. 51 (13) (2018) 134005.
[36] B. Zhao, R. Zhang, Z. Huang, B. Wang, Effect of the size of Cu clusters on selectivity and activity of acetylene selective hydrogenation, Appl. Catal. A Gen. 546 (2017) 111–121.
[37] X. Shi, et al., Copper Catalysts in Semihydrogenation of Acetylene: From Single Atoms to Nanoparticles, ACS Catal. 10 (2020) 3495–3504.
[38] C. Saggese, N.E. Sánchez, A. Frassoldati, A. Cuoci, T. Faravelli, M.U. Alzueta, E. Ranzi, Kinetic modeling study of polycyclic aromatic hydrocarbons and soot formation in acetylene pyrolysis, Energy Fuel 28 (2) (2014) 1489–1501.
[39] A. Martin, I. Cozmuta, M.J. Wright, I.D. Boyd, Kinetic rates for gas-phase chemistry of phenolic-based carbon ablator in atmospheric air, J. Thermophys. Heat Transf. 29 (2015) 222–240.
[40] T. Butterworth, A. van de Steeg, D. van den Bekerom, T. Minea, T. Righart, Q. Ong, G. van Rooij, Plasma induced vibrational excitation of CH_4 - A window to its mode selective processing, Plasma Sources Sci. Technol. 29 (9) (2020) 095007.
[41] P.-A. Maitre, M.S. Bieniek, P.N. Kechagiopoulos, Modelling excited species and their role on kinetic pathways in the non-oxidative coupling of methane by dielectric barrier discharge, Chem. Eng. Sci. 234 (2021) 116399.
[42] N. Pourali, V. Hessel, E.V. Rebrov, The Effects of Pulse Shape on the Selectivity and Production Rate in Non-oxidative Coupling of Methane by a Micro-DBD Reactor, Plasma Chem. Plasma Process. 42 (2022) 619–640.